The macro-structural variability of the human neocortex

Frithjof Kruggel [*]

Department of Biomedical Engineering, University of California, Irvine, USA

ABSTRACT

The human neocortex shows a considerable individual structural variability. While primary gyri and sulci are found in all normally developed brains and bear clear-cut gross structural descriptions, secondary structures are highly variable and not present in all brains. The blend of common and individual structures poses challenges when comparing structural and functional results from quantitative neuroimaging studies across individuals, and sets limits on the precision of location information much above the spatial resolution of current neuroimaging methods. This work aimed at quantifying structural variability on the neocortex, and at assessing the spatial relationship between regions common to all brains and their individual structural variants. Based on structural MRI data provided as the "900 Subjects Release" of the Human Connectome Project, a data-driven analytic approach was employed here from which the definition of seven cortical "communities" emerged. Apparently, these communities comprise common regions of structural features, while the individual variability is confined within a community. Similarities between the community structure and the state of the brain development at gestation week 32 lead suggest that communities are segregated early. Subdividing the neocortex into communities is suggested as anatomically more meaningful than the traditional lobar structure.

Introduction

The current neuro-anatomical ontology (NeuroNames, 2010; Swanson, 2015) is based on the traditional abstraction from visual observation rather than quantitative, data-driven evidence. Considerable training is required for a human observer to recognize neocortical structures. Difficulties arise from the well-known fact that even primary macro-anatomical features show a remarkable structural variability, and secondary features may be prevalent in some individuals only. An abundance of neuro-anatomical literature describes detailed variation (e.g., of the operculum: Ayberk et al., 2012; Idowu et al., 2014; or sulcal patterns: Ono et al., 1990). However, a quantitative assessment of variation patterns is missing that may lead to a deeper understanding of the relationship between common and variable structures on the human neocortex.

This variability renders approaches for an automated quantification of neocortical structures as difficult. Digital brain atlases have been developed to aid the communication and registration of neuro-scientific information with increasing levels of sophistication (Brett et al., 2001; Evans et al., 2012; Shattuck et al., 2008; Talairach and Tournoux, 1988). These image-based approaches contain exemplary, generic information with (some) population-based but not individual variation. Manual

outlining is still considered as the reference method for a precise segmentation of brain structures. Diligent procedures were developed that guide the delineation of macroscopic anatomy in individual brains (Klein and Tourville, 2012; Shattuck et al., 2008).

In contrast, several approaches were developed to represent anatomically meaningful, individual features of the neocortical surface in symbolic format. Most notably, Regis et al. (1995, 2005) introduced the concept of "sulcal roots" (or "pits") that correspond to locally deepest points of neocortical sulci. Lohmann and von Cramon (2000) developed a method for segmenting cortical patches as catchment basins centered at a sulcal roots. In a later publication, Lohmann et al. (2008) used gyral landmarks to define a common anatomical framework, into which sulcal pits were mapped. They describe 11 regional groups of major (deep) pits, and a larger set of minor (shallow) pits. Im et al. (2014) proposed a more refined approach to segment sulcal pits, and used a surface-based nonlinear atlas of sulcal patterns to map pits into a common space on a unit sphere. They selected deep pits manually, and segregated a map of 48 pit clusters that may serve as stable anatomical landmarks. We and others (Cachia et al., 2003; Yang and Kruggel, 2008) developed systems that use a derived network of neocortical patches to detect and label neocortical landmarks by symbolic pattern matching and learning processes. Auzias et al. (2013, 2015) picked up an idea already indicated by

* 202 Rockwell Engineering Center, University of California, Irvine, CA 92697-2755, USA.
  E-mail address: fkruggel@uci.edu.

Lohmann et al. (2008) that sulcal pits are arranged in concentric chains along the anterior-posterior axis of the brain, folding into the temporal lobe. They propose a longitude/latitude scheme between an insular and a cingular pole for parameterizing the neocortical surface, and devise a nonlinear mapping to align sulcal bottom lines across individuals.

It has long been noted that deep primary convolutions of the neocortex develop first, and are less variable than more shallow, secondary folds that appear later (for a review, refer to Welker, 1990), suggesting that the development of primary structures is under tighter genetic control. While mathematical modeling (Toro and Burnod, 2005) demonstrated that the development of cortical convolutions is a consequence of cortical growth, the development of thalamo- and cortico-cortical connections determine the segregation of neocortical space (e.g., Rakic, 1988, 2004; Welker, 1990), and contribute to the definition of the folding pattern. Thus, it has been hypothesized that deep sulcal pits develop first and are more invariant than shallow ones across individuals. The early structural development of the human brain was recently studied by in utero MRI (Dubois et al., 2008; Habas et al., 2012). The study of cortical curvature maps derived from this imaging data confirm that major folds develop between gestation week 22 and 28. Meng et al. (2014), analyzed data acquired in a large-scale longitudinal study of the cortical development in infants from 0 to 2 years of age, and studied spatial distribution and temporal development of deep sulcal landmarks in a critical period of brain development. A recent study confirmed a genetic influence on the formation of sulcal pits (Le Guen et al., 2017), albeit with moderate heritability estimates between 0.2 and 0.5.

Several studies (Lohmann et al., 2008; Im et al., 2014; Meng et al., 2014; Nie et al., 2012; Auzias et al., 2015) used sulcal pits as landmarks on the cortical surface. All employed different nonlinear registration procedures to reduce the inter-individual variability for deriving clusters of sulcal pits. The analytic approach described here retained the individual variability, and avoided using arguable features or anatomical models underlying nonlinear registration procedures. To quantify structural patterns, we segmented the neocortical surface into disjoint patches centered around pits, termed basins (Yang and Kruggel, 2008). Basins capture local surface properties such as patch size, surface curvature, geodesic depth, and neighborhood relationships with adjacent basins, thus, provide a richer representation than just the location information of sulcal pits. We represented the neocortical surface as a graph of basins linked by their neighborhood relationships, and analyzed the local variation of corresponding basin labels across a large subject sample to characterize cortical regions in terms of their structural variability. Using a two-level clustering approach, we determined seven groups of "co-varying" basins, called communities here, that emerge from the data without injecting anatomical knowledge. We hypothesized that communities form a structural layer between a hemisphere and its basins, such that communities are similar in all normally developed brains, while the inter-individual variability is kept within a community.

Methods and materials

In the following, we describe the image data base of the population sample used in this study, the processing that led to the segmentation of white matter (WM)/grey matter (GM) interfaces, the basin segmentation process, and the clustering method from which the definition of basin communities emerged.

Subjects and imaging data

This work included imaging data of all 897 subjects in the "900 Subjects Release" of the Human Connectome Project released in December 2015. This sample consists of 503 females and 394 males in the age range of 20–40 years. Structural MR images were acquired on a customized Siemens 3T "Connectome Skyra" housed at Washington University in St. Louis, using a standard 32-channel Siemens receive head coil and a body transmission coil. T1-weighted data were acquired using a 3D MPRAGE protocol with parameters TR = 2400 ms, TE = 2.14 ms, TI = 1000 ms, flip angle 8°, FOV = 224 × 224 mm, 0.7 mm isotropic voxel size, 7 min 40 s acquisition time. T2-weighted data were acquired using a 3D T2-space protocol with parameters TR = 3200 ms, TE = 565 ms, FOV = 224 × 224 mm, 0.7 mm isotropic voxel size, 8 min 24 s acquisition time. For detailed information, refer to the release document (Human Connectome Project, 2017).

Image processing

Our processing started from triangulated meshes representing the WM/GM interface of the left or right cerebral hemisphere with a topological genus of zero. Such surfaces can be generated by several available software packages, and we described our processing chain below.

Unprocessed T1-and T2-weighted structural images were downloaded from the HCP database server. Imaging data were converted from NIFTI to BRIAN format (Kruggel, 2017). Each T1-weighted image was aligned with the stereotaxic coordinate systems and the corresponding T2-weighted image rigidly registered with the aligned data set. Both images were corrected for intensity inhomogeneities (Glasser et al., 2013). A mask for the intracranial compartment was generated based on the T1-weighted image using a registration approach (Hentschel and Kruggel, 2004) and applied to both images. The intracranial space was classified into four compartments based on a Gaussian mixture model (He et al., 2008), roughly corresponding to WM, GM, cerebro-spinal fluid (CSF) and connective tissue. The inner cavities of the WM segmentation (ventricles and basal ganglia) were filled via a patch-based approach using an atlas of 20 pre-segmented data sets (Coupe et al., 2011). From the resulting WM segmentation of the brain, the cerebellum and brain stem were clipped at a level of 15 mm below the plane of the anterior and posterior commissures, and split into hemispheres at the mid-sagittal plane. In each hemisphere, a multi-seeded region growing process (Segonne, 2008) was applied to reconstruct the object as a single c_{18}-connected component (Toriwaki and Yonekura, 2002). A triangulated surface was computed from this object (Nielson, 2003), and optimally adapted to the WM/GM interface as a deformable model using the intensity-corrected T1-weighted brain image. Meshes retained the individual dimensions in which images were acquired ($\approx$ 1 mm vertex distance), and had a topological genus of zero. Each face represented an area of about 0.30 mm^2, each vertex a Voronoi area of about 0.60 mm^2 (Meyer et al., 2002).

Basin segmentation

The neocortical surface was segmented into patches using surface curvature and geodesic depth as local properties. Basins are regions grown from locally deepest points in convex regions at sulcal bottoms until they meet in concave regions at gyral crowns. We used a segmentation procedure that was revised from a previous publication (Yang and Kruggel, 2008).

Principal curvature components κ_1, κ_2 (Meyer et al., 2002) were computed at each vertex of the triangulated surface (see Fig. 1, top left) and converted into the shape index $s = \frac{2}{\pi} \arctan \frac{\kappa_1 + \kappa_2}{\kappa_1 - \kappa_2}$, that ranges between −1 (convex areas) and +1 (concave areas). For computing the geodesic depth, we used the hemispheric WM segmentation, filled sulci using a morphological closing operator, and computed a constrained distance transform on the difference image (Verbeek et al., 1986). The resulting depth values were interpolated in voxel space at vertex locations of the hemisphere mesh (see Fig. 1, top right).

The region growing process was seeded at locally deepest vertices, and each seed was addressed a unique label. In each iteration, all unlabeled vertices on the outer boundary of a region were examined, and the deepest vertex in a convex neighborhood was added to a region. The growing process ended when all vertices in a convex neighborhood were
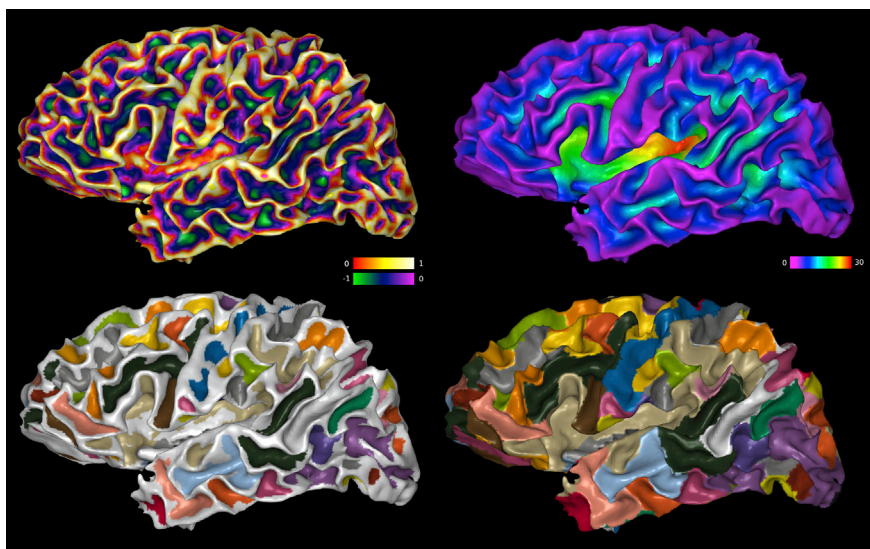
Fig. 1. Processing stages for basin segmentation: Surface curvature (top left, dimensionless units), geodesic depth (top right, in mm), initial basin segmentation (below left, arbitrary color labels), and final segmentation (below right, arbitrary color labels).

assigned to a region. Next, regions that included less than *lim* vertices were merged with a neighbor if (a) there was a single neighbor only, or (b) both regions shared a large fraction *fr* of their border (see Fig. 1, below left). Finally, regions were grown into concave areas until all surface vertices were labeled (see Fig. 1, below right). In order to keep regions compact, the closest unlabeled vertex in a concave neighborhood was selected in each iteration. Note that WM regions that were clipped at the mid-sagittal plane and the brain stem were excluded from the growing process. The final number of basins is dependent on the setting of the merge size limit *lim*, and, to a lesser extent, on the boundary length limit *fr*. Small regions form in the first step of the growing process (a) at shallow surface "dimples" or (b) in highly curved sulcal areas. Parameter setting were chosen as $lim = 200$ and $fr = 0.1$ to retain the first group but merge the second. This process yielded 80–120 basins per hemisphere and required about 8 s of processing time for a surface mesh of 150.000 vertices.

Neocortical variability

To assess the structural variability of the cortical surface, we mapped all basin segmentations of a specific hemisphere into the same space, and examined the overlap of basin regions. Invariant cortical locations (as referenced by a vertex positions) receive the same basin label, while variable locations receive several different labels.

The first step unfolded a hemisphere surface mesh onto a unit sphere. This mapping problem has been studied extensively (Clarenz et al., 2004). Mapping a convoluted surface onto a sphere introduces an error in the edge length and angles of the mapped triangles. Because it is important here to retain both size and shape of basins, we aimed at a minimal overall distortion (Friedel et al., 2007) and used a multi-resolution context for optimization (Kruggel, 2008). Note that mapped meshes retain their basin labels.

Next, the overall correspondence between spherical meshes was optimized by linear registration with an arbitrary reference. Technically, we optimized the free parameters of a quaternion rotation in 3D by maximizing the normalized mutual information of the vertex-wise labels. Given the best rotation parameters, labels of the object mesh were interpolated at vertex locations of the reference. As a result, basin labels of all hemispheric meshes were mapped onto locations of the reference mesh, thus, allowing point-to-point comparisons across all individuals. This linear matching retained most of the inter-subject variability, which is understood here as the variation of features found at a given position. It is sufficient to keep labels and other surface featurs of all hemispheric meshes as multi-valued vectors of the same length N_L, and retain the

vertex graph of the reference mesh to represent the connectivity.

Now, our variability metric can be defined. While the registration process led to an optimal overlap of basins, basin labels at any location may differ, due to inter-subject variability. For a reference sphere R with N_R distinct basin labels and a subject sphere S with N_S labels, we computed an $N_S \times N_R$ matrix of label correspondences. Element i, j of this matrix contained the number of vertices labeled as i on sphere S and j on sphere R. Thus, the basin i on S that best matches reference basin j can simply be found as the row-wise maximum. This map of homologue basins was used to relabel basins of S in terms of R. Given the same reference R, this process was repeated for all subject spheres S, accumulating N_R possible labels on S at each vertex i of the reference R in a matrix O of dimensions $N_L \times N_R$. Now, we respresented the distribution of labels at each vertex by a metric. For each row of this matrix, we ranked elements $O(i, j)$ by decreasing values, denoting the highest rank k as zero. For our variability metric V, we used the rank-weighted sum of region overlaps:

$$V_i = \sum_{j}^{N_R} k(O(i, j)) * O(i, j). \tag{1}$$

Note that the best match does not contribute to this sum ($k = 0$), such as non-overlapping basins ($O(i, j) = 0$). An optimal "one-on-one" overlap yields a variability of zero. A larger number of overlapping regions penalizes the metric by multiplication with an increasing rank k. Fig. 2 illustrates this procedure: all spherical basin meshes (top) were registered with a reference (below left), and variability scores computed by this process (below middle) were mapped onto an inflated reference surface mesh (below right) to ease identification of anatomical regions.

To be insensitive to the choice of the reference, each mesh was selected once as the reference, and the process above was repeated, resulting in 897 variability maps. To generate a common map, one mesh was selected as a reference, and nonlinear transformations from each mesh to this reference were computed, using the shape index as surface feature (Yeo et al., 2010). The resulting deformation fields were used to transfer all variability maps into a common space, and averaged.

Neocortical communities

The variability map introduced above provides a localized, vertex-wise measure of cortical variability. Now, we wanted to assess the extent by which basins overlap with neighbors across a subject sample, therefore, providing a regional assessment of cortical variability. We hypothesized that covarying basins show a stronger overlap and can be
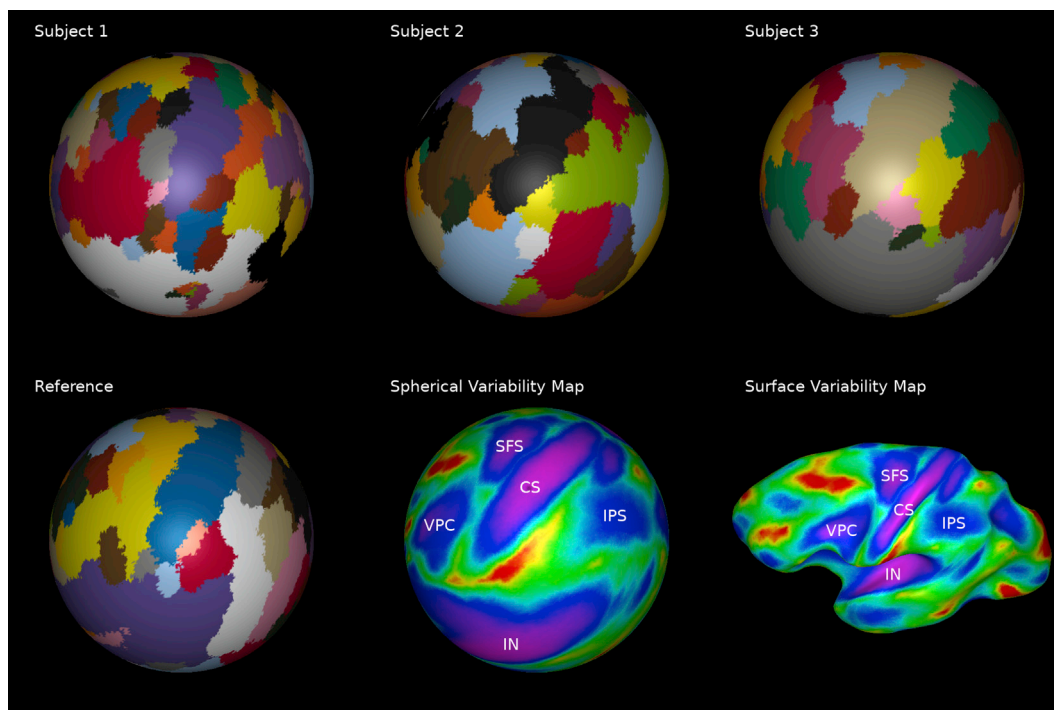
Fig. 2. Illustration of the process used to generate a variability map. All meshes correspond to the left brain hemisphere as seen from the left side. Top row: Basin segmentations of three subjects, mapped onto a sphere and registered with the basin map of a reference subject (below left). The resulting variability map for this reference subject is shown (below middle), along with the corresponding mapping on a surface mesh (below right). Several regions of low variability are labeled to ease orientation on the spheres. For explanation of the labels, refer to Fig. 5.

clustered into groups, called communities here.

Algorithmically, community building corresponds to a clustering process operating on a graph (for a review, refer to Fortunato, 2008). Here, nodes of this graph correspond to basins of a reference mesh. Initially, this graph is unconnected. For a chosen reference mesh R, labels on a subject mesh S were re-labeled as described above, to find a matrix O of dimensions $N_R \times N_R$ that contains the occurrence of label correspondencies. Elements on the diagonal of this matrix contain the counts of homologue labels between the reference and the subject mesh, and off-diagonal elements the amount of overlap between two non-homologue basin pairs. For each off-diagonal non-zero matrix element, an edge was added to the graph, and the edge weight updated by the amount of overlap. Given the same reference R, this process was repeated for all subject meshes S, accumulating edge weights w on the reference graph. At the end of this process, edge weights reflected the "connection strength" between neighboring basins as determined from the whole sample. Now, communities c were built by forming subsets of nodes that maximized their common connectivity while minimizing their cross-community connectivity. More formally, we aimed at maximizing the modularity:

$$M = \frac{1}{w_t} \sum_i^{N_R} \sum_j^{N_R} \left(O(i,j) - \frac{w_i w_j}{w_t} \right) \delta(c_i, c_j), \qquad (2)$$

where

$$w_t = \sum_i^{N_R} \sum_j^{N_R} O(i,j), \quad w_i = \sum_k^{N_R} O(i,k), \quad w_j = \sum_j^{N_R} O(k,j), \qquad (3)$$

and the delta function $\delta(\cdot)$ is equal to one if basins i and j were addressed to the same community.

Different approaches for this NP-hard problem have been developed. The optimal solution can be found by linear programming (Brandes et al., 2008), which may be prohibitive in terms of computation time when the number of basins N_R becomes large. Heuristic approaches form communities by agglomeration: initially, each node corresponds to a

community, and communities are merged until modularity is optimal. We used an algorithm (Campigotto et al., 2014) that randomizes an initial solution for a defined number of iterations while keeping the best overall solution. Note that the final number of communities N_C emerges from the optimization process. If two surfaces have an identical basin structure, the number of communities corresponds to the number of basins ($N_C = N_R$), if they are maximally different, just one community is found. For our problem, the optimal solution was found in 10–200 min of computation time (Brandes et al., 2008), while the heuristic solution was found in a few seconds (Campigotto et al., 2014), with a modularity score that was 1–2% lower than the optimal value.

Each mesh was selected once as the reference, and the process above was repeated, resulting in 897 maps of community clusters. The integration of all cluster maps into a common one is described in the next section. The similarity of two clustering maps can be determined from the co-occurrence matrix of the vertex-wise correspondences between community labels. The normalized mutual information (NMI) of this matrix was used as a similarity metric: this value ranges between 0 (for random label pairings) and 1 (for a vertex-wise identical community segmentation).

Results

Neocortical surface and basins

Basin segmentations were computed for both hemispheres in all 897 subjects included in this study. Between 100 ± 11.2 basins were found on the left, and 100 ± 10.5 on the right hemisphere (see Fig. 3), with no difference between hemispheres (paired t-test: $p = 0.855$). On average, males had 8.2 more basins on the left ($p < 0.0001$), and 7.7 more basins on the right hemisphere ($p < 0.0001$).

The total hemispheric surface area followed a normal distribution, after separating for sex: females $814 \pm 69 \, \text{cm}^2$ (left), $806 \pm 70 \, \text{cm}^2$ (right); males $924 \pm 77 \, \text{cm}^2$ (left), $913 \pm 79 \, \text{cm}^2$ (right). Hemispheric
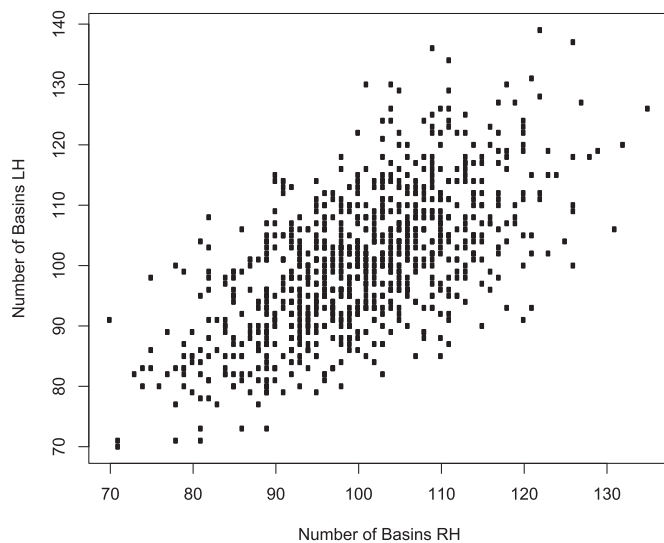
Fig. 3. Number of basins on the right (x axis) and left (y axis) hemisphere, where each dot corresponds to at least one subject. Overall, no statistical difference in the number of basins between hemispheres was found.

surfaces were slightly larger of the left vs right side in females ($+7.39\,cm^2$, 0.91%, paired t-test: $p < 0.0001$); and in males ($+10.38\,cm^2$, 1.12%, paired t-test: $p < 0.0001$). Our values are slightly lower compared to published data (Tramo et al., 1995; van Essen et al., 2012), because their results were given for a pial (Tramo) resp. mid-cortical surface segmentation (van Essen). Published relative variances (in percent) and male/female differences were similar to our results.

For each individual, basins were classified based on their size and maximum depth using a Gaussian mixture model, where the optimal number of classes was determined from the Bayesian information criterion (Fraley and Raftery, 2002). Individual class means were pooled among all subjects, and re-classified. Basins roughly group into three classes (refer to Fig. 4): (1) large, deep basins (avg. depth 15 mm, avg.
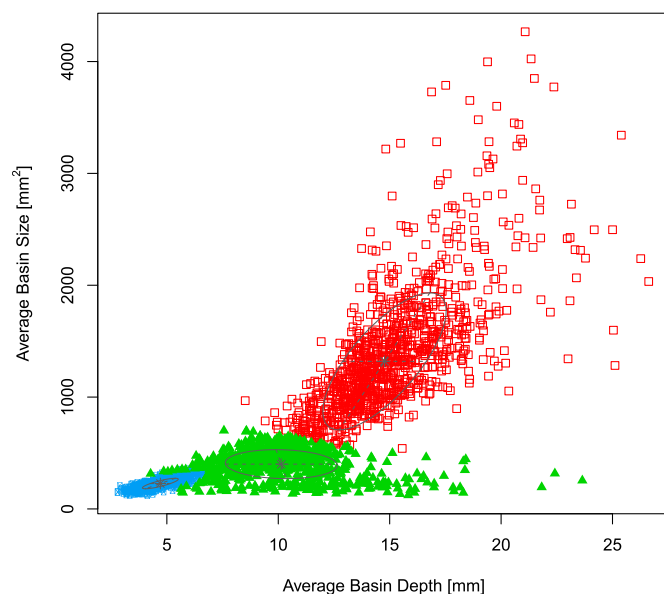

Fig. 4. Area vs. depth of basin classes on all left hemispheres. In a first approximation, three clusters can be distinguished: (1) large, deep basins (avg. depth 15 mm, avg. size $1320\,mm^2$), identified sections of primary sulci; (2) medium-sized, deep basins (avg. depth 10 mm, avg. size $400\,mm^2$), identified as sections of secondary sulci; (3) small, shallow basins (avg. depth 4.7 mm, avg. size $230\,mm^2$), corresponding to "dimples".

size $1320\,mm^2$), identified sections of primary sulci; (2) medium-sized, deep basins (avg. depth 10 mm, avg. size $400\,mm^2$), identified as sections of secondary sulci; (3) small, shallow basins (avg. depth 4.7 mm, avg. size $230\,mm^2$), corresponding to "dimples".

Neocortical variability

Variability scores were determined for both hemispheres, including all 897 subjects. Fourteen regions were found as invariant that were roughly similar in extent and variability scores in both hemispheres (see Fig. 5, magenta-blue regions):

(1) the insula (IN), (2) the central sulcus (CS), (3) the ventral segment of the pre-central sulcus (PCS), (4) the dorsal segment of the pre-central sulcus, extending into the superior frontal sulcus (SFS), (5) the ventral segment of the post-central sulcus (IPS), extending into the anterior section of the intra-parietal sulcus, (6) the caudal section of the intra-parietal sulcus (CIP), (7) the superior temporal sulcus (STS), (8) the olfactory sulcus, (9) the orbital sulci (ORS, OLS), (10) the anterior portion of the collateral sulcus (ACS), (11) the posterior section of the collateral fissure (PCS), (12) the marginal portion and knee of the cingulate sulcus (MCS), (13) the precuneus (PC), (14) the parieto-occipital sulcus (POS).

Regions of highest variability (see Fig. 5, yellow-red regions) were found as a mesh of partially connected long rims: (1) along the edge between the lateral and medial surface of both hemispheres, from the frontal to the occipital pole, (2) along the trajectory of the inferior temporal gyrus from the occipital to the temporal pole, (3) from the occipital pole to the inferior parietal lobule, splitting into two branches (a) along the dorsal margin between the insula and the lateral surface, to the frontal pole, and (b) along the ventral margin between the insula and the lateral surface, to the temporal pole.

Neocortical communities

Now, basin segmentations were clustered into neocortical communities. Community maps were computed for each subject, resulting in 897 maps for both hemispheres. Note that the number of communities emerges from the clustering process. For all subjects included here, a relatively narrow range of 7–13 communities per hemisphere were found (see Fig. 6). Modularity scores were in the order of 0.75, indicating a high degree of separation between communities.

The number of communities was not significantly different between both hemispheres of a subject (paired Wilcoxon-test: $p = 0.320$), and did not depend on sex, surface size, or the number of basins.

To examine the community structure across all subjects, a two-step procedure was used. First, the pair-wise similarity of two community maps was expressed by the NMI of the label co-occurrence matrix. Similarity values followed a narrow, unimodal Gaussian distribution: 0.71 ± 0.03, indicating a high similarity among all pairs of community structures. Then, pairwise similarity values were compiled in matrix and converted into a Euclidean distance matrix. A principal component analysis was used to map distances into a low-dimensional space consisting of 10 dimensions with 90.2% retained variance. Classification using a Gaussian mixture model revealed that all solutions belong to a single cluster.

Second, a variability map of all community labelings was computed, similar to the process described for the basin labelings above. Regions of low variability (magenta) correspond to communities consistently found in all subjects (see Fig. 7), bordered by rims of high variability (green-red). Clear separations between communities indicated a highly similar community pattern on all hemispheres. The variability map was segmented using a watershed-region growing procedure into seven communities in each hemisphere.

To ease orientation, communities were mapped onto a reference surface mesh (see Fig. 8). The basic layout consists of seven communities, identified as: (1) an orbital region including the frontal pole and orbital portion of the frontal lobe (OR); (2) a frontal region including structures
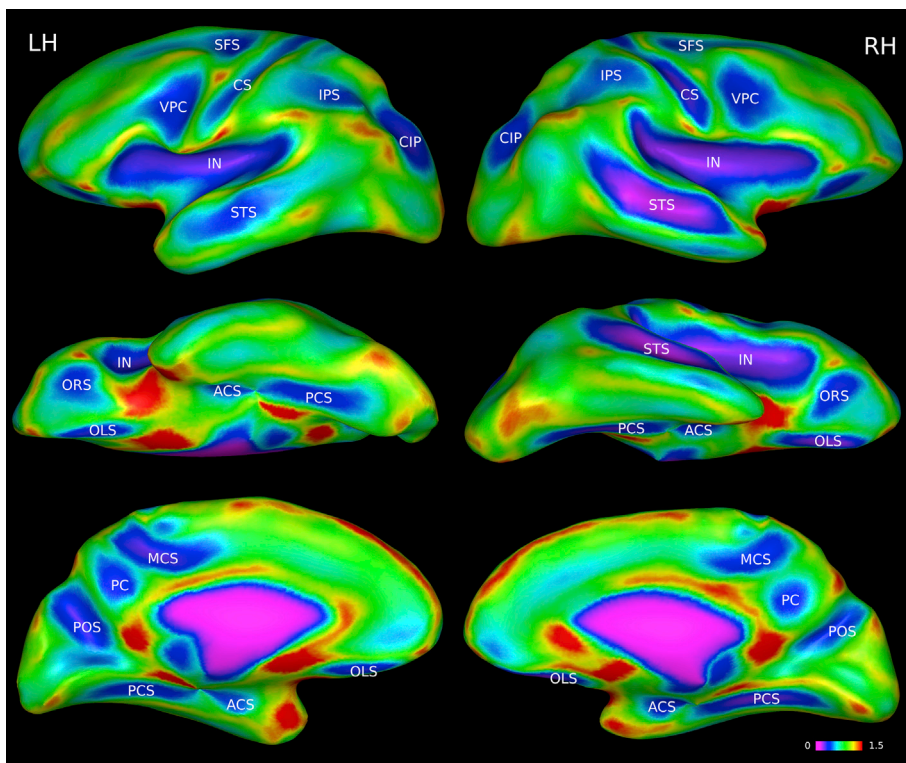
Fig. 5. Vertex-wise variability for both hemispheres, collected in 897 subjects and mapped onto an inflated reference surface. Higher values indicate more variable regions. Fourteen regions (in magenta-blue) were detected as invariant: (IN) the insula, (CS) the central sulcus, (VPC) the ventral segment of the pre-central sulcus, (SFS) the dorsal segment of the pre-central sulcus, extending into the superior frontal sulcus, (IPS) the ventral segment of the post-central sulcus, extending into the anterior section of the intra-parietal sulcus, (CIP) the caudal section of the intra-parietal sulcus, (STS) the superior temporal sulcus, (OLS) the olfactory sulcus, (ORS) the orbital sulci, (ACS) the anterior portion of the collateral sulcus, (PCS) the posterior section of the collateral fissure, (MCS) the marginal portion and knee of the cingulate sulcus, (PC) the precuneus, (POS) the parieto-occipital sulcus.
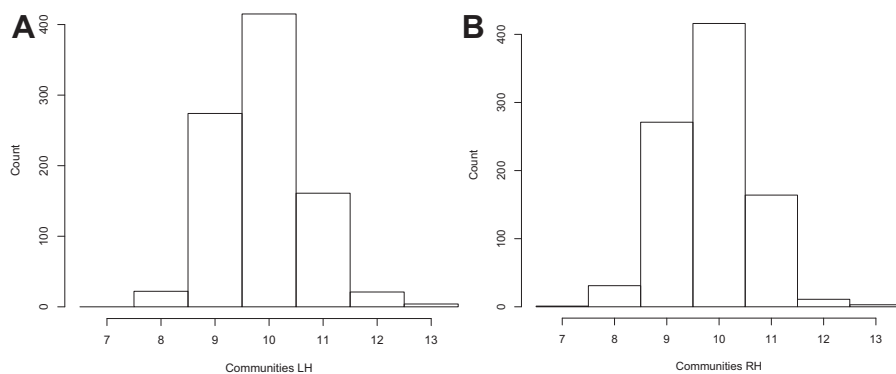

Fig. 6. Number of hemispheres found per number of detected communities on the left (A) and right hemisphere (B).
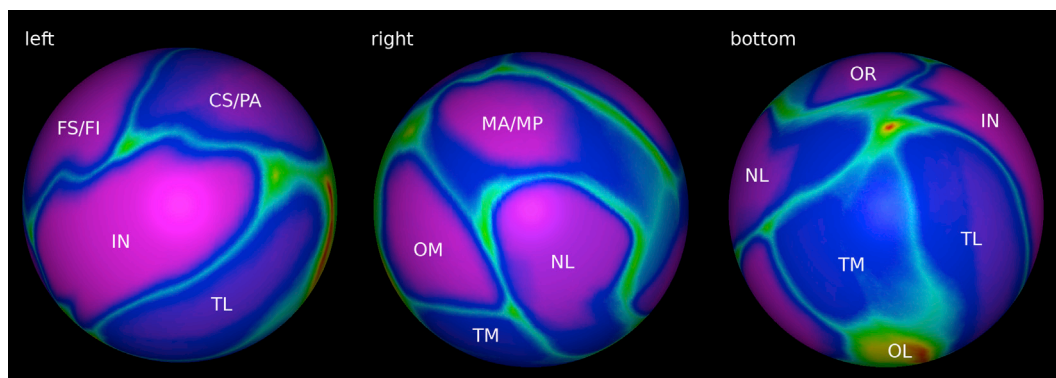

Fig. 7. Variability map computed from community clustering. Communities can be identified as regions of low variability (magenta), bordered by rims of high variability (green-red). All meshes correspond to the left brain hemisphere, as seen from the left (left figure), right (middle figure), and bottom (right figure). For explanation of the labels, refer to Fig. 8.
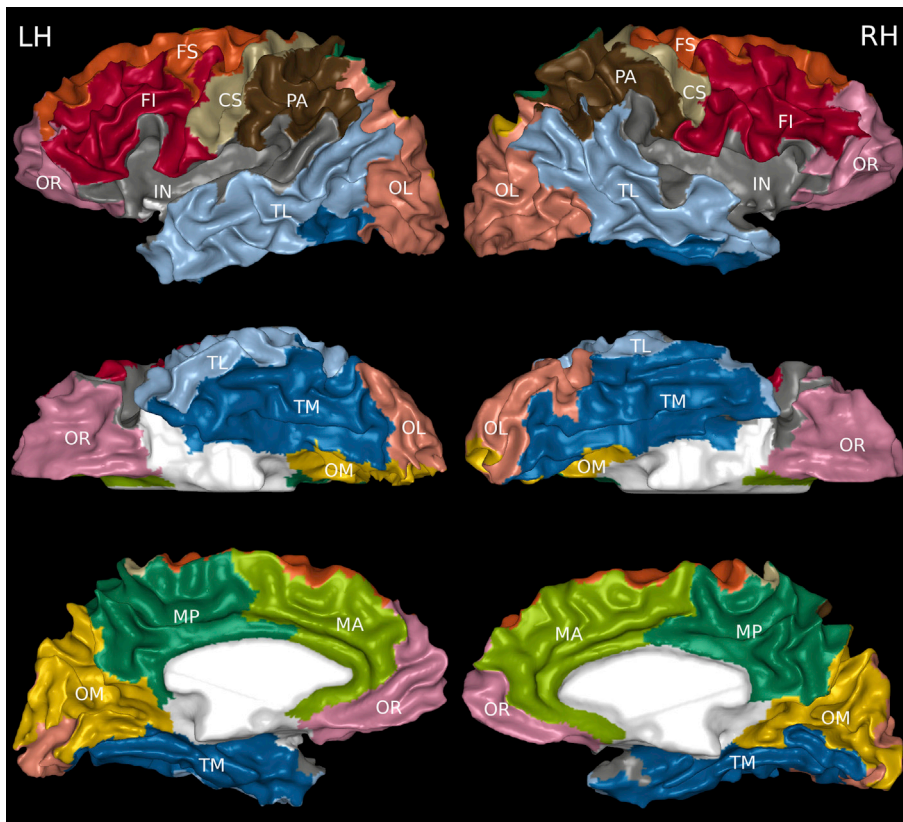
Fig. 8. Basin communities for both hemispheres, derived from 897 subjects, shown for an example reference mesh. Generally, seven communities were found: orbital (OR, 1, in pink); fronto-superior (FS, 2a, in orange) and fronto-inferior (FI, 2b, in red); central sulcus (CS, 3a, light brown) and parietal (PA, 3b, in dark brown); insula (IN, 4, in grey); temporo-lateral (TL, 5a, in light blue) and temporo-medial (TM, 5b, in dark blue); occipito-lateral (OL, 6a, in coral) and occipito-medial (OM, 6b, in yellow); medial-anterior (MA, 7a, in light green) and medial-posterior (MP, 7b, in dark green). Rarely, the insula is split into an anterior and posterior portion. Communities marked as (a,b) may not be separated in some hemispheres, resulting in a range of 7–13 communities per hemisphere.

on the lateral convexity of the frontal lobe (FI, FS); (3) a central region corresponding to the central, post-central and intra-parietal sulcus and adjacent gyri (CS, PA); (4) the insula including the frontal and parietal operculum (IN); (5) a temporal region (TL, TM); (6) an occipital region (OL, OM); and (7) the medial surface including the cingulate sulcus and precuneus (MA,MP). Medial cut planes and the brain stem were addressed to community NL.

Next, each of these basic communities was compared with the individual community structure, again using overlap matrices. Five communities were often split: the frontal region into a more regular inferior (2a, FI) and more variable superior portion (2b, FS); the centro-parietal into a central (3a, CS) and parietal portion (3b, PA); the temporal region into a clearly separated lateral (5a, TL) and medial portion (5b, TM); the occipital into a regular medial (6a, OM), and a highly variable lateral portion (6b, OL), and the medial region into a more regular posterior (7a, MP) and variable portion anterior portion (7b, MA). Rarely, the insula is

split into an anterior and posterior portion. Any combination of these splits may be found in a specific hemisphere, leading to the variation of the number of communities shown in Fig. 6.

The high similarity of the community structure across individuals may be surprising. However, comparing the figures for the vertex-wise similarity (Fig. 5) and the community structure (Fig. 8) demonstrated that communities were formed around regions of low variability: the orbital region around ORS and OLS; the frontal regions around SFS and VPC; the centro-parietal region around CS and IPS; the temporal regions around STS and (ACS,PCS); and the occipital regions around CIP and POS. The yellow-red rims in Fig. 5 approximately corresponded to the boundaries of the communities in Fig. 8.

Areas of the individual communities were analyzed for sex-related and inter-hemispheric differences (see Table 1). Roughly, communities took similar proportions of the total hemispheric surface, with MA the smallest (LH, 4.2%) and TL the largest (LH, 11.9%) community.

Table 1

Community area, relative area difference (male vs. female) and significance (*t*-test) for communities on the left and right hemisphere; relative area difference (left vs. right) and significance (paired *t*-test). Areas and differences Δ are specified in % of the total surface area of a given hemisphere. Community NL corresponds to the surface area on the cut planes. Results were suppressed for non-significant (n.s.) comparisons, at a threshold of $p = 0.05$.

Community	Size LH	Δ(M/F)	*p*-value	Size RH	Δ(M/F)	*p*-value	Δ(LH/RH)	*p*-value
NL	5.99	−0.300	<0.0001	6.00	−0.244	<0.0001	–	n.s.
FS	7.32	–	n.s.	7.25	–	n.s.	–	n.s.
FI	8.81	0.251	7.22e-4	7.65	0.170	0.0191	1.160	<0.0001
CS	4.42	−0.122	9.61e-3	4.23	–	n.s.	0.186	<0.0001
PA	6.12	–	n.s.	7.05	–	n.s.	0.929	<0.0001
MA	4.15	0.241	1.23e-3	5.78	–	n.s.	−1.625	<0.0001
MP	6.58	−0.170	0.0315	6.08	–	n.s.	0.494	<0.0001
IN	11.85	–	n.s.	10.45	−0.250	<0.0001	1.400	<0.0001
TL	11.02	–	n.s.	9.23	–	n.s.	1.783	<0.0001
TM	10.18	−0.156	0.0250	10.25	–	n.s.	–	n.s.
OL	8.39	–	n.s.	10.78	–	n.s.	−2.38	<0.0001
OM	7.24	–	n.s.	7.71	0.218	<0.0001	−0.461	<0.0001
OR	7.87	0.138	0.0294	7.49	0.142	0.0212	0.382	<0.0001

Significant inter-hemispheric differences were found for 10/14 communities: OL (RH > LH, 2.38%); TL (LH > RH, 1.78%); MA (RH > LH, 1.63%); IN (LH > RH, 1.40%); FI (LH > RH, 1.16%); PA (RH > LH, 0.93%); MP (LH > RH, 0.49%); OM (RH > LH, 0.61%); OR (LH > RH, 0.38%); and CS (LH > RH, 0.19%). Comparatively minor, but statistically significant sex-related differences in community area were found for 4/14 communities: IN (females > males, 0.25%); OM (males > females, 0.22%); FI (males > females, 0.17%); and OR (males > females, 0.14%).

In a first approximation, communities FI, FS, OR, and MA correspond to the surface of the frontal lobe, communities CS, PA, and MP to the parietal lobe, communities TL, TM to the temporal lobe, and communities OL, OM to the occipital lobe. This is further illustrated in Table 2.

Brain hemispheres were segmented into lobes using the MNI structural atlas (Mazziotta et al., 2001). Lobe labels were mapped onto surface meshes, and the amount of overlap between lobes and the combinations of communities above was assessed. Note that lobe boundaries were defined by convention, and (mostly) follow sulcal bottom lines, while communities were determined by a data-driven approach, and are bounded by gyral crowns.

Discussion

This work assessed the variability of the macroscopic structures of the human neocortex using a data-driven approach. We employed the concept of cortical basins that implicitly encodes local surface properties, i.e., curvature and geodesic depth. To compare across individuals, we mapped cortical surfaces onto a common sphere while optimally retaining the shape, size and neighborhood relationships of basins. Variability was determined from the set of different basin labels that map onto a specific surface location, weighted by their probability. Using the amount of mutual overlap of basins across individuals, we grouped basins into seven communities that are structurally segregated. Several methodological and neuro-biological issues are discussed in the following.

Methodology

Basin Segmentation: We used the concept of basins to parcellate the neocortical surface: a basin corresponds to a patch of the neocortical surface centered around a locally deepest point ("pit"), bordered by a local ridge (Lohmann and von Cramon, 2000; Yang and Kruggel, 2008). Although in terms of data processing, basins are straightforward and robust to segment, two details deserve discussion: (1) We assessed different criteria for the basin merging process that influence the number and size of basins retained for further processing. While the concept of basins introduced above holds well for the convexity of the hemisphere, shallow sulci on the medial frontal lobe and sulci adjacent to the limen insulae require less rigorous criteria. After a comprehensive study, we decided to merge adjacent regions if their common border in a convex region is longer than 10% of the perimeter of the smaller region. (2) As an alternative to our basin approach, the cortical segmentation can be

started from gyral crest lines (Stylianou and Farin, 2004), and grow regions into sulci. However, gyral crest lines form a complex, connected mesh that must be split into segments while sulcal roots are naturally separated. Such a gyral segmentation defines structural units in terms of gyri, with boundaries at sulcal bottom lines. Gyral segmentations also arise if cortical end points of white matter fiber tracts are used for parceling the neocortex, as discussed below. Here, we favored the sulcal/basin approach due to its simplicity and robustness.

Spherical Mapping: To compare structural features across individuals, we mapped hemispheric surfaces onto a unit sphere. This process introduces (1) an overall linear spatial normalization due to difference in brain size, and (2) a regional nonlinear deformation related to individual structural properties. Quantifying possible issues of the analytic procedure is difficult due to the unknown amount of individual differences. To estimate the error introduced by the spherical mapping, we selected region NL (i.e., the excluded vertices), and compared the relative area on the spherical vs. hemisphere mesh in an individual data set. For the left side, we found a ratio of 0.991 [0.976–1.001], for the right side 0.973 [0.962–0.985], indicating that the typical error in area size is less than 3%. Thus, the choice of our mapping metric ensured that local area (and shape) were well reproduced in the spherical map. Next, we assessed the similarity between region NL in an individual map registered to the reference map by computing the Jaccard index (the ratio of the intersection and the union of both regions). For the left side, we found an index of 0.680 [0.622–0.735], for the right side 0.712 [0.662–0.758], corresponding to an overlap of 81–83%. These lower values and wider margins express the influence of the individual variability retained by the mapping process. Likewise, we conclude that the individual variability in region size is much larger than the error introduced by the nonlinear mapping process.

As an alternative to spherical mapping, a recent approach for assessing the variability of cortical features could be used (Awate et al., 2016, 2017). This method uses a regional histogram-based descriptor of cortical measures (GM thickness, curvedness and shape index) to establish robust and optimal correspondencies across a set of surface meshes, and offers the advantage of providing a statistical assessment of cortical features. Structural features can also be matched in frequency space (Auzias et al., 2013; Lombaert et al., 2013). This approach leads to point-to-point correspondences between individual meshes with gradual significance. Although this procedure avoids scaling and mapping issues discussed here, the relevance and validity of such correspondences for providing insight into structural variability is not clear. We consider the normalization approach used here as rather simple and straightforward to understand.

Variability Measure: We introduced a vertex-wise measure to represent structural variability. By construction, this summary measure includes probabilistic information about the number of different basins found at this location and their relative prevalence. We also sampled vertex-wise the probability that a vertex receives one basin label only and assessed local indicators of spatial association (using Moran's I: Anselin, 1995).

Table 2
Comparison between a segmentation into lobes (vertical) vs. combinations of communities (horizontal) for the left (top) and right hemisphere (below). Values are given in % of the total spherical surface and are averaged over all subjects. Note that values do not add up to 100% due to the presence of cut planes (NL label). For more information, please, refer to the text.

Lobe	FS + FI + OR + MA	CS + PA + MP	TL + TM	OL + OM	IN
frontal	28.20	0.40	0.02	0.00	0.00
parietal	3.25	13.75	0.04	0.19	0.00
temporal	0.18	1.65	14.00	5.15	0.01
occipital	0.00	2.97	0.06	13.02	0.00
insula	3.36	3.48	3.57	0.03	1.07
Lobe	FS + FI + OR + MA	CS + PA + MP	TL + TM	OL + OM	IN
frontal	27.82	0.61	0.02	0.00	0.00
parietal	2.74	14.58	0.00	0.13	0.00
temporal	0.02	3.01	13.46	2.33	0.00
occipital	0.00	4.27	1.29	13.18	0.00
insula	2.69	2.71	3.39	0.00	1.30

This measure detects spatial clusters, here, of structural variability. The resulting statistical map was highly similar to Fig. 5 and did not reveal additional information.

Conceptually, our approach for assessing variability differs from other published methods. If two hemispheres differ in scale and orientation only, they will be mapped identically onto the spherical mesh. Any differences in local scale and shape are retained as individual differences because our procedure does not include a regional matching, e.g., based on surface features. Replacing our method of spatial normalization through parametrization with a nonlinear registration approach (e.g., Awate et al., 2016, 2017; Auzias et al., 2013; Lombaert et al., 2013; Yeo et al., 2010) would likely lead to a "sharper" variability map, at the expense of defining a criterion for defining correspondencies between cortical regions. However, we doubt that the range of variability values will be much affected, because the number of neighboring basins is independent of the mapping process.

Our rank-based variability measure tolerates a "mild" variability. Consider the central sulcus that is often represented by a single basin, and sometimes split into two. If this split occurs in 20% of all cases, the variability measure is 0.2. If three basins were found at a given vertex with rates 60%, 20%, and 20%, the variability measure increases to 0.6. Thus, the variability measure highlights areas where there or more basins were found at similar rates. It should also be emphasized that variability is computed vertex-wise, and does not assess (conventional) sulcal structures. Consider the superior temporal sulcus that is often mapped onto three or four basins with considerable differences in orientation. As long as not more than two basins overlap at a given vertex, the variability is not greater than 0.5. Conversely, in regions such as the middle cingular sulcus or the operculum insulae, the application of the basin concept is arguable, and potentially leads to an "inflated" variability.

Community Clustering: The high degree of modularity found in the clustering process is not surprising. Our data are natively embedded on a two-dimensional surface, limiting the number of possible interacting neighbors. Because it is expected that surface structures never switch places, the number of viable basin arrangements is further reduced. The alternative community splits described in Section 3.3 have modularity values that differ by a 1–2% only. Therefore, we prefer to postpone a final decision about the "best" number of communities, other than stating a lower bound of seven.

Neurobiology

Relevance of Basins: It is well established that sulcal pits are reliable cortical landmarks and are helpful for abstracting from the inter-individual variability (Cachia et al., 2003; Im et al., 2014; Lohmann et al., 2008; Meng et al., 2014; Regis et al., 2005; Yang and Kruggel, 2008). Instead of point landmarks, we used surface patches in terms of basins in this analysis, that implicitly encode the spatial extent of a region surrounding a local pit, and its orientation and neighborhood relationships with other basins on the neocortical surface, thus, retain a richer set of information. While both approaches are equivalent and are expected to yield similar results, we aimed at a complete parcellation of the neocortical surface.

A strong positive correlation between basin size and depth was found here (see Fig. 4). We interpreted this as a consequence of the fact that all basins must accommodate a cortical layer of a similar thickness. In a first approximation, basins cluster into three classes: (1) large, deep basins, identified sections of primary sulci; (2) medium-sized, deep basins, identified as sections of secondary sulci; (3) small, shallow basins, corresponding to "dimples". We found a total of 80–120 basins per hemisphere; removing shallow ones reduced the number of basins to 50–60, which is in line with previous studies that focused on deep pits (Im et al., 2014: 48/47 regions; Meng et al., 2014: 54 regions; Regis et al., 2005: 57 regions). The same number of basins was found in both hemispheres, as reported by Meng et al. (2014).

Clustering of Basins: Several studies used variants of nonlinear registration procedures to reduce the inter-individual variability, and to find a common set of deepest local pits in spatial "concentration regions" (Lohmann et al., 2008; Im et al., 2014; Meng et al., 2014; Regis et al., 2005). In contrast, we retained in the individual variability in our analysis and assessed which basins covary to form communities. Thus, communities correspond to surface patches that include one or more concentration regions in the sense above and provide a hierarchical organization level below a hemisphere but above basins/pits. We consider the set of seven communities outlined here as common to all normally developed brains, and hypothesize that individual variation is confined within a community. A quantitative assessment of the individual variability within communities is subject to future work (see also Meng et al., 2014).

Communities showed a left-ward asymmetry for PA, IN, and TL and a right-ward asymmetry for OL and MA (see Table 1). The sign and magnitude of these asymmetries are in line with published data (Lyttelton et al., 2009; van Essen et al., 2012), although both publication show vertex-wise instead of region area statistics provided here. Sex-related differences in community size found here were on an order of magnitude smaller than inter-hemispheric differences. Available data on the sign and magnitude of sex-related differences in surface size are sparse and inconclusive (e.g., Escoriala et al., 2015). Although some of these differences were statistically significant, doubts may be raised whether size differences in the order of 0.1% bear neuro-biological relevance. It should be noted that well-described sexual dimorphisms in brain structures (e.g., Ruigrok et al., 2014) were described at the level below our communities.

Variability and Brain Development: There is mounting evidence that the deepest basins (pits) are formed early in development (Dubois et al., 2008; Habas et al., 2012; Le Guen et al., 2017; Meng et al., 2014; Nie et al., 2012) and may serve as anchors for the development of functional areas (Rakic, 1988, 2004; Welker, 1990). We found a striking similarity of the cortical variability (see Fig. 5) with a reconstruction of the cortical surface of a preterm newborn imaged at gestational week 32 (Dubois et al., 2008, see Fig. 9). The regions of lowest variability correspond to the sulcal regions formed first during development. We hypothesize that basin communities correspond to this common core expressed in all brains before individual determinants of brain development dominate. Basins formed later are more shallow and have a higher degree of individual structural variability.

This hypothesis is in line with recent models of cortical development. Toro and Burnod (2005) found that primary sulci are likely determined by (a) the location of architectonic inhomogeneities (Welker, 1990), presumably influenced by region-specific genetic regulation (Johnson et al., 2009; Rakic, 2004) and (b) mechanical influences on the initial geometry of the cortex, such as exerted by differential growth patterns of ontogenetic columns (Rakic, 1988). Secondary and ternary folds develop subsequently as mandated by the preceding primary convolutions.
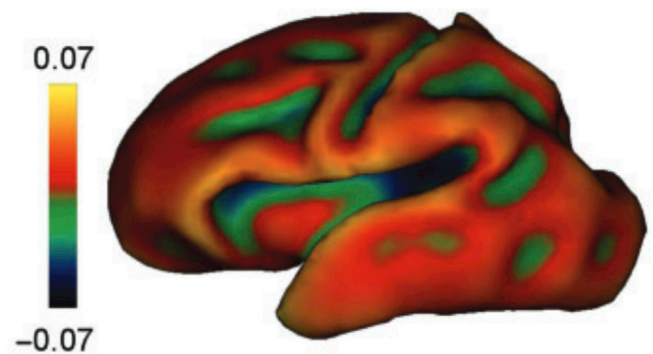

Fig. 9. Reconstruction of the WM/GM surface of a preterm newborn imaged at gestational week 32. Color codes correspond to the surface curvature. Image was taken from Dubois et al. (2008, Fig. 1e).

Communities and Vascular Supply: We also note that there is a close correspondence between communities and vascular territories of the main cerebral arteries (Tatu et al., 1998): the anterior cerebral artery supplies communities OR, MA, and MP; the middle cerebral artery supplies communities FI, FS, IN, CS, PA and TL; while the posterior cerebral artery supplies communities OL, OM, and TM. We suggest that the separation into cortical communities provides a more natural, data-driven route for referencing cortical structures than one based on lobes.

Cortical Connectivity: Another support for the notion of communities may come from the study of basin connectivity through cortico-cortical WM fibers. The first description of sulcal interruptions ("plis de passage") was provided by Gratiolet in 1854 that consist of short-range U-fibers bridging a sulcus. A cortical parcellation based on white matter structures was developed by Oishi et al. (2008), and led to the definition of nine white matter "blades" that introduce a cortical segmentation based on gyral stalks. Although their analysis does not follow a data-driven approach, the resulting regions are roughly similar to our communities. Hagmann et al. (2008) performed a network analysis of individual structural connectivity maps directly, leading to a partitioning of 66 anatomical subregions. Nijhuis et al. (2013) defined "cortical hubs" as locations with higher long-range inter-connectivity. While all three approaches provided an elegant and clear-cut analysis of connectivity data, they strived to find and segregate patterns common to a population sample from individual variation. We were unable to find studies that assess basins and their connectivity.

The concept of basin communities introduced here extends and supersedes previous structural clustering approaches based on sulcal roots. By construction, communities are formed around local regions of low inter-subject variability. The demonstrated similarity of communities with the developing folding pattern at week 32 suggests the hypothesis that communities are segregated early, and that the subsequent individual development is confined within a community. We propose that our data-driven approach led to an anatomically (and presumably, functionally) more meaningful subdivision of the neocortex than the traditional concept of lobes. This suggestion is corroborated by the fact that vascular supply patterns match easily with the community but not with the lobe architecture. Further research will elucidate whether there are distinguishable basin patterns within a community that may be related to the presence of structural variants (e.g., the presence of a diagonal sulcus), providing a route for the quantification of individual surface structures.

References

Anselin, L., 1995. The local indicators of spatial association – LISA. Geogr. Anal. 27, 93–115.

Auzias, G., Lefevre, J., Le Troter, A., Fischer, C., Perrot, M., Regis, J., Coulon, O., 2013. Model-driven harmonic parameterization of the cortical surface: HIP-HOP. IEEE Trans. Med. Imag. 32, 873–887.

Auzias, G., Brun, L., Deruelle, C., Coulon, O., 2015. Deep sulcal landmarks: algorithmic and conceptual improvements in the definition and extraction of sulcal pits. Neuroimage 111, 12–25.

Awate, S.P., Leahy, R.M., Joshi, A.A., 2016. Riemannian statistical analysis of cortical geometry with robustness to partial homology and misalignment. In: Ourselin, S., et al. (Eds.), Medical Image Computing and Computer-assisted Intervention. MICCAI 2016, vol. 9900. Springer, Cham, pp. 237–246. Lecture Notes in Computer Science.

Awate, S.P., Leahy, R.M., Joshi, A.A., 2017. Kernel methods for Riemannian analysis of robust descriptors of the cerebral cortex. In: Niethammer, M., et al. (Eds.), Information Processing in Medical Imaging. IPMI 2017, vol. 10265. Springer, Cham, pp. 28–40. Lecture Notes in Computer Science.

Ayberk, G., Yagli, E., Comert, A., Esmer, A.F., Canturk, N., Tekdemir, I., Dinc, H., 2012. Anatomic relationship between the anterior sylvian point and the pars triangularis. Clin. Anat. 25, 429–436.

Brandes, U., Delling, D., Gaertler, M., Gorke, R., Hoefer, M., Nikoloski, Z., Wagner, D., 2008. On modularity clustering. IEEE Trans. Knowl. Data Eng. 20, 172–188.

Brett, M., Christoff, K., Cusack, R., Lancaster, J., 2001. Using the Talairach atlas with the MNI template. Neuroimage 13, S85.

Cachia, A., Mangin, J.F., Riviere, D., Kherif, F., Boddaert, N., Andrade, A., Papadopoulos-Orfanos, D., Poline, J.B., Bloch, I., Zilbovicius, M., Sonigo, P., Brunelle, F., Regis, J., 2003. A primal sketch of the cortex mean curvature: a morphogenesis based approach to study the variability of the folding patterns. IEEE Trans. Med. Imag. 22, 754–765.

Campigotto, R., Cespedes, P.C., Guillaume, J.L., 2014. A generalized and adaptive method for community detection. arVix, 1406.2518v1.

Clarenz, U., Litke, N., Rumpf, M., 2004. Axioms and variational problems in surface parameterization. Comput. Aided Geomet. Des. 21, 727–749.

Coupe, P., Manjon, J.V., Fonov, V., Pruessner, J., Robles, M., Collins, D.L., 2011. Patch-based segmentation using expert priors: application to hippocampus and ventricle segmentation. Neuroimage 54, 940–954.

Dubois, J., Benders, M., Borradori-Tolsa, C., Cachia, A., Lazeyras, F., Ha-Vinh Leuchter, R., Sizonenko, S.V., Warfield, S.K., Mangin, J.F., Hüppi, P.S., 2008. Primary cortical folding in the human newborn: an early marker of later functional development. Brain 2028–2041. https://doi.org/10.1093/brain/awn137.

Escoriala, S., Roman, F.J., Martinez, K., Burgaleta, M., Karama, S., Colomb, R., 2015. Sex differences in neocortical structure and cognitive performance: a surface-based morphometry study. Neuroimage 104, 355–365.

Evans, A.C., Janke, A.L., Collin, D.L., Baillet, S., 2012. Brain templates and atlases. Neuroimage 62, 911–922.

Fortunato, S., 2008. Community detection in graphs. Phys. Rep. 486, 75–174.

Fraley, C., Raftery, A.E., 2002. Model-based clustering, discriminant analysis and density estimation. J. Am. Stat. Assoc. 97, 611–631.

Friedel, I., Schroeder, P., Desbrun, M., 2007. Unconstrained spherical parameterization. J. Graph., GPU, Game Tools 12, 17–26.

Glasser, M.F., Sotiropoulos, S.N., Wilson, J.A., Coalson, T.S., Fischl, B., Andersson, J.L., Xu, J., Jbabdi, S., Webster, M., Polimeni, J.R., van Essen, D.C., Jenkinson, M., 2013. The minimal preprocessing pipelines for the Human Connectome Project. Neuroimage 80, 105–124.

Gratiolet, P.L., 1854. Memoire sur les plis cerebraux de l'homme et des primates. Bertrand, Paris, France.

Habas, P.A., Scott, J.A., Roosta, A., Rajagopalan, V., Kim, K., Rousseau, F., Barkovich, A.J., Glenn, O.A., Studholme, C., 2012. Early folding patterns and asymmetries of the normal human brain detected from in utero MRI. Cerebr. Cortex 20, 13–25.

Hagmann, P., Cammoun, L., Gigandet, X., Meuli, R., Honey, C.J., Wedeen, V.J., Sprons, O., 2008. Mapping the structural core of human cerebral cortex. PLoS Biol. 6, e159. https://doi.org/10.1371/journal.pbio.0060159.

He, R., Datta, S., Sajja, B.R., Narayana, P.R., 2008. Generalized fuzzy clustering for segmentation of multi-spectral magnetic resonance images. Comput. Med. Imag. Graph. 32, 353–366.

Hentschel, S., Kruggel, F., 2004. Determination of the intracranial compartment: a registration approach. In: Jiang, T. (Ed.), Medical Imaging and Augmented Reality (Beijing), Lecture Notes in Computer Science, vol. 3150. Springer, Singapore, pp. 253–260.

Human Connectome Project. 900 Subjects Data Release Reference. https://www.humanconnectome.org/documentation/S900/HCP_S900_Release.pdf (accessed: November 1, 2017).

Idowu, O.E., Soyemi, S., Atobatele, K., 2014. Morphometry, asymmetry and variations of the sylvian fissure and sulci bordering and within the pars triangularis and pars operculum: an autopsy study. J. Clin. Diagn. Res. 8, AC11–AC14.

Im, K., Jo, H.J., Mangin, J.F., Evans, A.C., Kim, S.I., Lee, J.M., 2014. Spatial distribution of deep sulcal landmarks and hemispherical asymmetry on the cortical surface. Cerebr. Cortex 20, 602–611.

Johnson, M.B., Kawasawa, Y.I., Mason, C.E., Krsnik, Z., Coppola, G., Bogdanovic, D., Geschwind, D.H., Mane, S.M., State, M.W., 2009. Functional and evolutionary insights into human brain development through global transcriptome analysis. Neuron 62, 494–509.

Klein, A., Tourville, J., 2012. 101 labeled brain images and a consistent human cortical labeling protocol. Front. Neurosci. https://doi.org/10.3389/fnins.2012.00171.

Kruggel, F., 2008. Robust parametrization of brain surface meshes. Med. Image Anal. 12, 291–299.

Kruggel, F., 2017. THE BRIAN system. https://sip.eng.uci.edu (accessed: November 1, 2017).

Le Guen, Y., Auzias, G., Leroy, F., Noulhiane, M., Dehaene-Lambertz, G., Duchesnay, E., Mangin, J.F., Coulon, O., Frouin, V., 2017. Genetic influence on the sulcal pits: on the origin of the first cortical folds. Cerebr. Cortex 1–12.

Lohmann, G., von Cramon, D.Y., 2000. Automatic labelling of the human cortical surface using sulcal basins. Med. Image Anal. 4, 179–188.

Lohmann, G., von Cramon, D.Y., Colchester, A.C., 2008. Deep sulcal landmarks provide an organizing framework for human cortical folding. Cerebr. Cortex 18, 1415–1420.

Lombaert, H., Grady, L., Polimeni, J.R., Cheriet, F., 2013. FOCUSR: feature oriented correspondence using spectral regularization - a method for precise surface matching. IEEE Trans. Pattern Anal. Mach. Intell. 35, 2143–2160.

Lyttelton, O.C., Karama, S., Ad-Dab'bagh, Y., Zatorre, R.J., Carbonell, F., Worsley, K., Evans, A.C., 2009. Positional and surface area asymmetry of the human cerebral cortex. Neuroimage 46, 895–903.

Mazziotta, J., Toga, A., Evans, A., Fox, P., Lancaster, J., Zilles, K., Woods, R., Paus, T., Simpson, G., Pike, B., Holmes, C., Collins, L., Thompson, P., MacDonald, D., Iacoboni, M., Schormann, T., Amunts, K., Palomero-Gallagher, N., Geyer, S., Parsons, L., Narr, K., Kabani, N., Le Goualher, G., Boomsma, D., Cannon, T., Kawashima, R., Mazoyer, B., 2001. A probabilistic atlas and reference system for the human brain: international Consortium for Brain Mapping (ICBM). Royal Soc. Phil. Trans. B 356, 1293–1322.

Meng, Y., Li, G., Lin, W., Gilmore, J.H., Shen, D., 2014. Spatial distribution and longitudinal development of deep cortical sulcal landmarks in infants. Neuroimage 100, 206–218.

Meyer, M., Desbrun, M., Schröder, P., Barr, A.H., 2002. Discrete differential-geometry operators for triangulated 2-manifolds. Visual. Math. 3, 1–26.

NeuroNames Ontology of Mammalian Neuroanatomy: NN2010 (2010). http://braininfo. rprc.washington.edu/nnont.aspx (accessed: November 1, 2017).

Nie, J., Li, G., Wang, L., Gilmore, J.H., Lin, W., Shen, D., 2012. A computational growth model for measuring dynamic cortical development in the first year of life. Cerebr. Cortex 22, 2272–2284.

Nielson, G.M., 2003. On marching cubes. IEEE Trans. Vis. Comput. Graph. 9, 283–293.

Nijhuis, E.H.J., van Cappellen van Walsum, A.M., Norris, D.G., 2013. Topographic hub maps of the human structural neocortical network. PLoS One 8, e65511. https:// doi.org/10.1371/journal.pone.0065511.

Oishi, K., Zilles, K., Amunts, K., Faria, A., Jiang, H., Li, X., Akhter, K., Hua, K., Woods, R., Toga, A.W., Pike, G.B., Rosa-Neta, P., Evans, A., Yhang, J., Huang, H., Miller, M.I., van Zijl, P.C.M., Mazziotta, J., Mori, S., 2008. Human brain white matter atlas: identification and assignment of common anatomical structures in superficial white matter. Neuroimage 43, 447–457.

Ono, M., Kubik, S., Abernathey, C.D., 1990. Atlas of the Cerebral Sulci. Thieme, Stuttgart.

Rakic, P., 1988. Specification of cerebral cortical areas. Science 241, 170–176.

Rakic, P., 2004. Genetic control of cortical convolutions. Science 303, 1983–1984.

Regis, J., Mangin, J.F., Frouin, V., Sastre, F., Peragut, J.C., Samson, Y., 1995. Generic model for the localization of the cerebral cortex and preoperative multimodal integration in epilepsy surgery. Stereotact. Funct. Neurosurg. 65, 72–80.

Regis, J., Mangin, J.F., Ochiai, T., Frouin, V., Riviere, D., Cachia, A., Tamura, M., Samson, Y., 2005. "Sulcal root" generic model: a hypothesis to overcome the variability of the human cortex folding patterns. Neurol. Med.-Chir. 45, 1–17.

Ruigrok, A.N.V., Salimi-Khorshidi, G., Lai, M.C., Baron-Cohen, S., Lombardo, M.V., Tait, R.J., Suckling, J., 2014. A meta-analysis of sex differences in human brain structure. Neurosci. Biobehav. Rev. 39, 34–50.

Segonne, F., 2008. Active contours under topology control–genus preserving level sets. Int. J. Comput. Vis. 79, 107–117.

Shattuck, D.W., Mirza, M., Adisetiyo, V., Hojatkashani, C., Salamon, G., Narr, K.L., Poldrack, R.A., Bilder, R.M., Toga, A.W., 2008. Delineation protocols for the LONI probabilistic brain atlas (LPBA40). Suppl. Doc. NeuroImage 39, 1064–1080.

Stylianou, G., Farin, G., 2004. Crest lines for surface segmentation and flattening. IEEE Trans. Vis. 10, 536–544.

Swanson, L., 2015. Neuroanatomical terminology: A lexicon of classical origins and historical foundations. Oxford University Press, Oxford, UK.

Talairach, J., Tournoux, P., 1988. Co-planar stereotactic atlas of the human brain: 3-dimensional proportional system: An approach to cerebral imaging. Thieme Verlag, Stuttgart.

Tatu, L., Moulin, T., Bogousslavsky, J., Duvernoy, H., 1998. Arterial territories of the human brain. Neurology 50, 1699–1708.

Toriwaki, J., Yonekura, T., 2002. Local patterns and connectivity indexes in a three dimensional digital picture. Forma 17, 275–291.

Toro, R., Burnod, Y., 2005. A morphogenetic model for the development of cortical convolutions. Cerebr. Cortex 15, 1900–1913.

Tramo, J.D., Loftus, W.C., Thomas, C.E., Green, R.L., Mott, L.A., Gazzaniga, M.S., 1995. Surface area of human cerebral cortex and its gross morphological subdivisions: in vivo measurements in monozygotic twins suggest differential hemisphere effects of genetic factors. J. Cognit. Neurosci. 7, 292–302.

van Essen, D.C., Glasser, M.F., Dierker, D.L., Harwell, J., Coalson, T., 2012. Parcellations and hemispheric asymmetries of human cerebral cortex analyzed on surface-based atlases. Cerebr. Cortex 22, 2241–2262.

Verbeek, P.W., Dorst, L., Verwer, B.J.H., Groen, F.C.A., 1986. Collision avoidance and path finding through constrained distance transformation in robot state space. In: Proceedings in Intelligent Autonomous Systems, pp. 634–641. Amsterdam, The Netherlands, Dec. 1986.

Welker, W., 1990. Why does cerebral cortex fissure and fold? A review of determinants of gyri and sulci. In: Jones, E., Peters, A. (Eds.), Cerebral Cortex, vol. 8b. Plenum Press, New York, pp. 3–136.

Yang, F., Kruggel, F., 2008. Automatic segmentation of human brain sulci. Med. Image Anal. 12, 442–451.

Yeo, B.T., Sabuncu, M.R., Vercauteren, T., Ayache, N., Fischl, B., Golland, P., 2010. Spherical demons: fast diffeomorphic landmark-free surface registration. IEEE Trans. Med. Imag. 29, 650–669.